All-Dielectric Layered Photonic Topological Insulators

*Xiao-Dong Chen, Xin-Tao He, and Jian-Wen Dong**

The recent realization of photonic topological insulators has brought the discovery of fundamentally new states of light and revolutionary applications such as nonreciprocal devices for photonic diodes and robust waveguides for light routing. The spatially distinguished layer pseudospin has attracted attention in two-dimensional electronic materials but it is yet to be discovered in topological photonic structures. Here, all-dielectric layered photonic topological insulators based on bilayer photonic crystal slabs are reported. The introduction of layer pseudospin offers more dispersion engineering capability, leading to the layer-polarized and layer-mixed photonic topological insulators. Their phase transition is demonstrated with a model Hamiltonian by considering the nonzero interlayer coupling. Layer-direction locking behavior of layer-polarized photonic topological insulators results in the selective light refraction. High transmission is observed in the bilayer domain wall between two layer-mixed photonic topological insulators, even when a large defect is introduced. Layered photonic topological insulators not only offer a route toward the observation of richer nontrivial phases, but also open a way for device applications in integrated photonics and information processing by using the additional layer pseudospin.

1. Introduction

Recently, the realization of classical analogues of topological insulators in artificial crystals has been an emerging research area.[1–9] Particularly in 2005, Haldane and Raghu transferred the key feature of topological insulators to the realm of photonics and proposed the photonic analog of quantum Hall effect in photonic crystals (PCs).[10,11] After this milestone of work, photonic analog of topological insulators, that is, photonic topological insulators (PTIs) have been theoretically proposed and experimentally demonstrated in different photonic systems.[12–24] Some traditional views on light propagation were overturned with the application of topological concepts. For example, broadband nonreciprocal propagation of light was realized,[10–12] and reflection-free routing of light along sharply bent waveguides was demonstrated.[16,17] By borrowing the discrete degrees of freedom (e.g., spin and valley), the advent of PTIs has opened a path toward the discovery of fundamentally new states of light and revolutionary photonic devices. Take the photonic analog of graphene as an example, there are two valleys of bulk bands at the corners of the Brillouin zone when the inversion (mirror) symmetry is broken.[17] Within these two valleys, the Berry curvatures are opposite.[22] Hence, valley binary degree of freedom is introduced to represent these two inequivalent energy extrema. Valley-Hall PTIs were found[17] and topologically protected refraction of kink states was demonstrated.[23]

On the other hand, the emergence of two-dimensional (2D) layered materials has provided a laboratory for exploring topologically nontrivial phases such as quantum Hall, spin Hall, and valley Hall phases.[25–28] In addition to the real electronic spin and valley pseudospin, the layer degree of freedom has been investigated as an additional pseudospin in bilayer systems.[29] A state localized to the upper or lower layer of bilayer graphene or transition metal dichalcogenides can be labeled with pseudospin up or down, respectively. The exploration of layer pseudospin and its interplay with other degrees of freedom has inspired numerous intriguing phenomena such as tunable gap bandwidth,[30] spin-layer locking effects,[31] magnetoelectric effects,[32] and unconventional superconductivity.[33] Recently, the layer pseudospin has been introduced into bilayer sonic crystals which consist of two layers of sonic crystals separated by a rigid plate and coupled through circular air channels.[34] Valley topological phases were discussed and various applications such as the layer-polarization converter for acoustics were experimentally demonstrated. However, the spatially distinguished layer pseudospin is yet to be discovered in topological photonic systems.

In this work, we report all-dielectric layered PTIs by introducing the layer pseudospin into bilayer PC slabs. The introduction of additional layer pseudospin offers more dispersion engineering capability and a model Hamiltonian is developed to describe the interlayer interaction within bilayer PC slabs. Layer-polarized and layer-mixed PTIs are realized, and their phase transition is demonstrated. Layer-direction locking behavior is found at the edge states between two layer-polarized PTIs, and it leads to the selective refraction of edge states when the position of incident source is switched. High transmission is achieved in the bilayer domain wall between two layer-mixed PTIs, even when a large defect is introduced. Layered PTIs open up a route toward the discovery of fundamentally novel states of light and applications such as layer-dependent light transmission.

Dr. X.-D. Chen, Dr. X.-T. He, Prof. J.-W. Dong
School of Physics & State Key Laboratory of Optoelectronic Materials and Technologies
Sun Yat-sen University
Guangzhou 510275, China
E-mail: dongjwen@mail.sysu.edu.cn

The ORCID identification number(s) for the author(s) of this article can be found under https://doi.org/10.1002/lpor.201900091

DOI: 10.1002/lpor.201900091

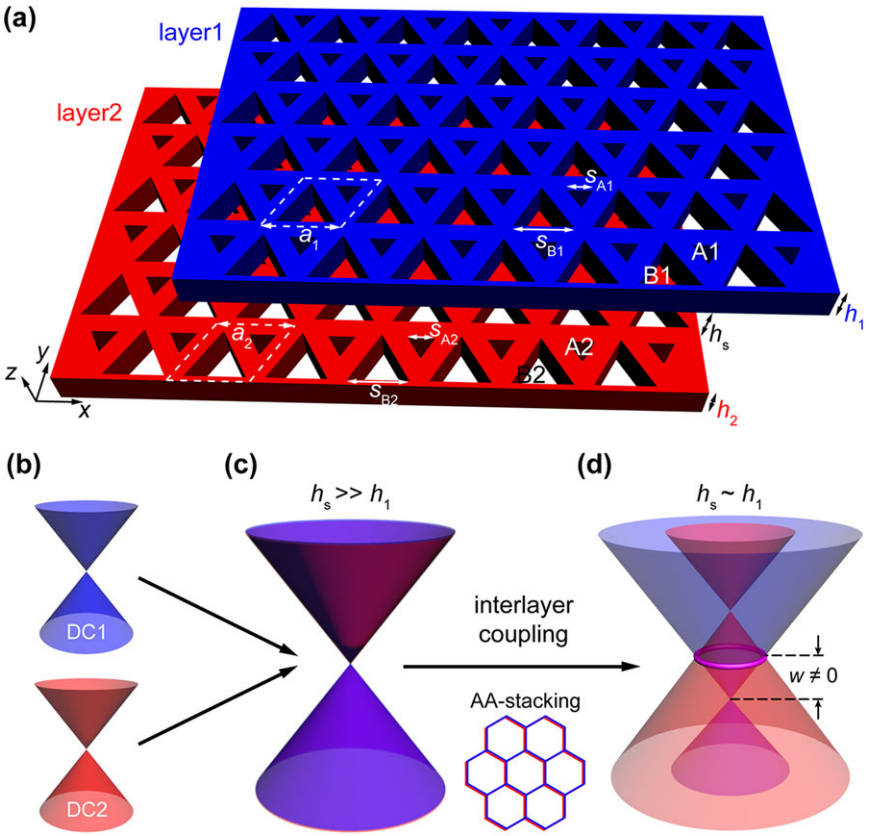

Figure 1. a) Schematic of an all-dielectric bilayer PC slab with the upper layer (layer1) shifting to show the lower layer (layer2). Each PC slab consists of a dielectric membrane ($\varepsilon = 12$) with a honeycomb lattice of triangular air-holes (i.e., A1 and B1 in layer1 while A2 and B2 in layer2). These two PC slabs are separated by a homogeneous spacer. Structural parameters: the lattice constant of PC slabs (a_1 and a_2), the thickness of two layers (h_1 and h_2), the thickness of spacer (h_s), the lateral size of triangular air-holes (s_{A1} and s_{B1}, s_{A2} and s_{B2}). Throughout this work, the subscripts of "1", "2," and "s" represent layer1, layer2, and spacer, respectively. b–d) Schematics of the evolution of double Dirac cones under the interlayer coupling. b) Transverse-electric like states of each slab form a gapless Dirac cone (DC) at the corner of Brillouin zone. c) Doubly degenerate Dirac cones occur when two slabs are far apart, that is, $h_s \gg h_1$. d) When the interlayer coupling is turned on (i.e., $w \neq 0$) for AA-stacking bilayer PC slabs, two Dirac cones are shifted oppositely along the frequency axis. A frequency nodal ring occurs around the K point (marked in pink), serving as an ideal starting point to have PTIs.

2. All-Dielectric Bilayer Photonic Crystal Slabs

We consider the all-dielectric bilayer PC slab which consists of two layers of PC slabs, that is, the upper layer1 and the lower layer2 (**Figure 1**a). They have the thickness of h_1 and h_2, and are separated by a homogeneous spacer ($\varepsilon = 1$) with the thickness of h_s. Each PC slab consists of a dielectric plate ($\varepsilon = 12$) with periodic air-holes with the lattice constants of a_1 and a_2. There are two equilateral triangular air-holes in the unit cell of each layer, that is, A1 and B1 in layer1 while A2 and B2 in layer2. The lateral sizes of the triangular air-holes in layer1 are s_{A1} and s_{B1}, while those in layer2 are s_{A2} and s_{B2}. Transverse-electric like (TE-like) states of each slab form a gapless Dirac cone at the corner of Brillouin zone (Figure 1b, and the detailed discussion is in Section A, Supporting Information). When $h_s >> h_1$, there is no interlayer coupling between two slabs and two Dirac cones are doubly degenerate (Figure 1c). When the interlayer coupling is turned on, the band dispersions of bilayer PC slabs can be engineered. In this work, we keep equal lattice constants of $a = a_1 = a_2$ and focus on the AA-stacking bilayer structure. When the thickness of spacer becomes comparative to those of the PC slabs (i.e., $h_s \approx h_1$), the electromagnetic fields of two slabs are coupled, leading to two oppositely shifted Dirac cones along the frequency axis (Figure 1d, and the detailed discussion is in Section C, Supporting Information). To see band dispersion engineering, we consider the AA-stacking bilayer PC slab with $a = 460$ nm, $h_1 = h_2 = h_s = 220$ nm, and equal air-hole sizes of $s_{A1} = s_{B1} = s_{A2} = s_{B2} = 250$ nm (inset of **Figure 2**a). These structural parameters are tuned to bring the bilayer PC slabs working at the telecommunication frequency around 200 THz (i.e., working wavelength around 1550 nm). Figure 2a shows its bulk band structure with $k_z = 0$, with the light cone shaded in gray. All eigenstates are labeled in colors by the polarization factor (i.e., M_z) which is calculated by averaging $\frac{|E_x|^2+|E_y|^2-|E_z|^2}{|E_x|^2+|E_y|^2+|E_z|^2}$ at the central plane of two layers, that is, $z = (h_1 + h_s)/2$ and $z = -(h_2 + h_s)/2$. Hence, TE-like modes are characterized by $M_z = 1$ and TM-like modes by $M_z = -1$. Under the light cone, two TE-like Dirac cones are separated along the frequency axis. Figure 2b illustrates H_z fields of four bulk states at the K point. Two degenerate mirror-symmetric

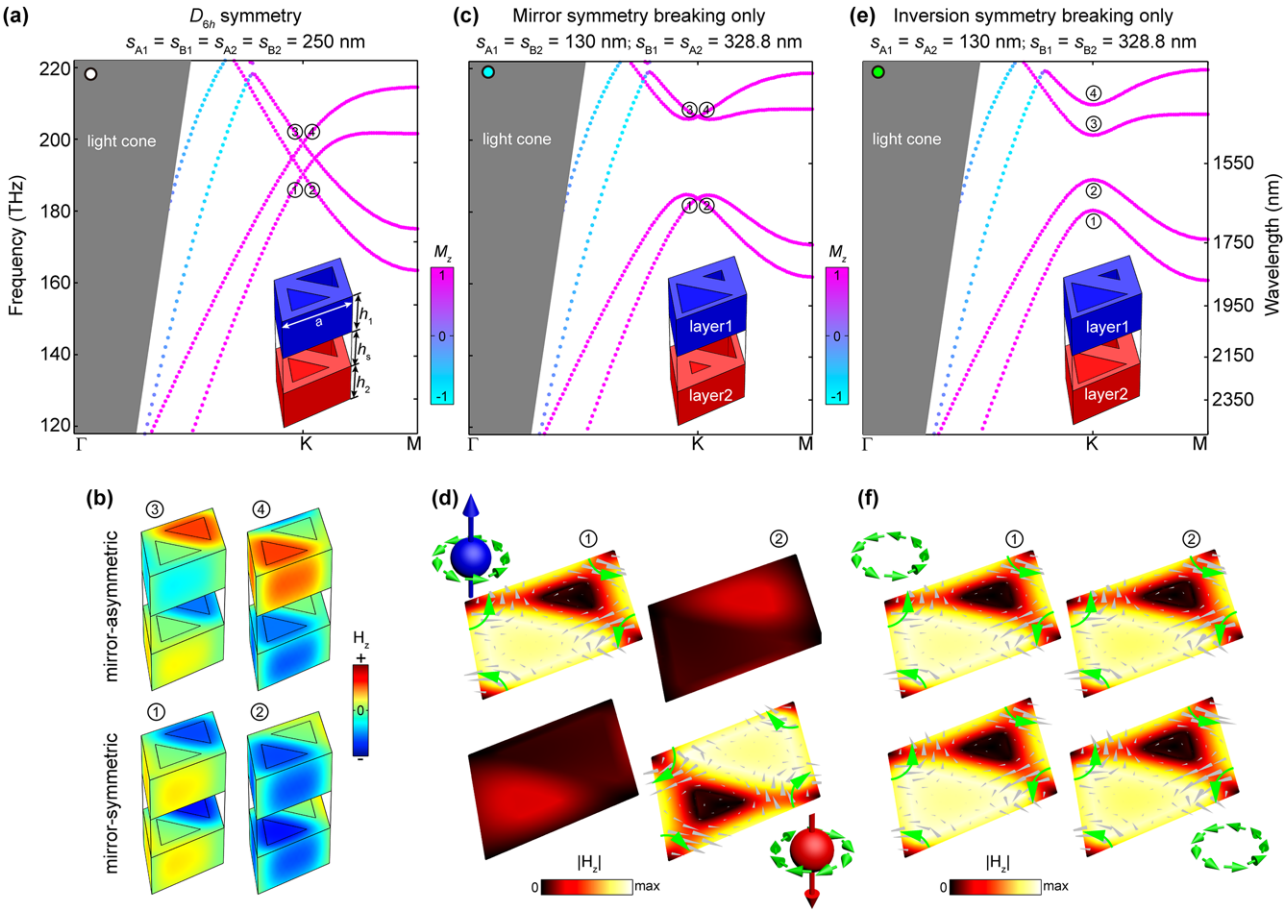

Figure 2. a–f) Bulk band structures and eigenfields of AA-stacking bilayer PC slabs without (a,b) and with (c–f) perturbations. The lattice constants are $a = a_1 = a_2 = 460$ nm, and the thicknesses of slabs and spacer are $h_1 = h_2 = h_s = 220$ nm. All states are marked in colors according to the polarization factor (M_z). The light cone is shaded in gray. The schematic of unit cell is shown in the inset. a) The D_{6h} symmetric PC slab with equal air-hole sizes of $s_{A1} = s_{B1} = s_{A2} = s_{B2} = 250$ nm has two frequency shifted Dirac cones and a frequency nodal ring enclosing the K point. b) Eigenfields (H_z) of four bulk states at the K point. Two mirror-symmetric (mirror-asymmetric) states appear at the lower (higher) frequency. c) The mirror symmetry breaking bilayer PC slab with $s_{A1} = s_{B2} = 130$ nm and $s_{B1} = s_{A2} = 328.8$ nm has a directional bandgap and two pairs of degenerate states at the K point. d) The absolute value of H_z (colors) and the power flux (gray arrows) at the central plane of layer1 and layer2 for two lowest bulk states at the K point. To guide the eye, schematic green arrows are added to indicate the rotation direction of the power flux. The twofold degeneracy is between the pseudospin-up anticlockwise state and pseudospin-down clockwise state (3D schematics), confirming the photonic analogue of spin–orbit coupling when the "layer" is treated as a pseudospin. e) The inversion symmetry breaking bilayer PC slab with $s_{A1} = s_{A2} = 130$ nm and $s_{B1} = s_{B2} = 328.8$ nm has a directional bandgap. f) The absolute value of H_z (colors) and the power flux (gray arrows) at the central plane of layer1 and layer2 for two lowest bulk states at the K point. To guide the eye, schematic green arrows are added to indicate the rotation direction of the power flux. These two states belong to the same orbital states (3D schematics).

states (① and ②) appear at the lower frequency, while two degenerate mirror-asymmetric states (③ and ④) show up at the higher frequency. Due to different mirror representations, these two cones cross with each other. It leads that a frequency nodal ring between the second and third bands encloses around the K point, serving as an ideal starting point to have PTIs.

3. Layered Photonic Topological Insulators

The all-dielectric bilayer PC slab presented in Figure 2a has the D_{6h} symmetry which contains the mirror symmetry (i.e., $(x, y, z) \rightarrow (x, y, -z)$) and the inversion symmetry (i.e., $(x, y, z) \rightarrow (-x, -y, -z)$). Layered PTIs can be obtained by applying symmetry breaking perturbations to this bilayer PC slab. We first discuss the structure where the mirror or inversion symmetry is broken individually, and then in next section consider the general case where mirror and inversion symmetries are broken simultaneously.

As shown in the inset of Figure 2c, we first consider the bilayer PC slab with $s_{A1} = s_{B2} = 130$ nm and $s_{B1} = s_{A2} = 328.8$ nm. For this structure, the inversion symmetry is preserved while the mirror symmetry is broken. The broken mirror symmetry leads to the repulsion between the second and third bands, and a resultant directional bandgap is obtained between the frequencies of 185.2 and 206.2 THz (i.e., wavelengths of 1620 and 1455 nm) (Figure 2c). Below the bandgap, there are twofold degenerate states at the K point. These two states have fields localizing at

different layers (Figure 2d). One state has H_z fields localizing at layer1 and power flux rotating anticlockwise (see in ①), while the other state has H_z fields localizing at layer2 and power flux rotating clockwise (see in ②). Hence, the twofold degeneracy is between the pseudospin-up anticlockwise state and pseudospin-down clockwise state when the *layer* is introduced as a pseudospin (3D schematics in Figure 2d). It is the photonic analogue of spin–orbit coupling, and we denote this resultant pseudospin-Hall PTI as the layer-polarized PTI.

We next consider the bilayer PC slab with $s_{A1} = s_{A2} = 130\,\text{nm}$ and $s_{B1} = s_{B2} = 328.8\,\text{nm}$ in which the mirror symmetry is preserved while the inversion symmetry is broken (inset of Figure 2e). Figure 2e shows its bulk band structure in which a directional bandgap is also found. Below the bandgap, both two bulk states at the K point have H_z fields mixing between two layers (Figure 2f). In addition, indicating by the same anticlockwise power fluxes (gray arrows), these two states belong to the same orbital states (3D schematics in Figure 2f). Here, we denote this kind of bilayer PC slab as the layer-mixed PTI.

4. Phase Transition and Effective Hamiltonian

The layer-polarized PTI in Figure 2c and the layer-mixed PTI in Figure 2e are distinct. We can simultaneously apply both mirror and inversion symmetry breaking perturbations to observe the phase transition between them. To do this, we consider the bilayer PC slabs with varied s_{A1} and s_{A2}. The amplitude of mirror (inversion) symmetry breaking is given by $\Delta = s_{A1}^2 - s_{A2}^2$ ($\Sigma = s_{A1}^2 + s_{A2}^2 - 125000\,\text{nm}^2$). In addition, we keep the same air-holes sizes at each slab, that is, $s_{A1}^2 + s_{B1}^2 = s_{A2}^2 + s_{B2}^2 = 125000\,\text{nm}^2$. This constant filling ratio condition ensures the dispersions of perturbed bilayer PC slabs do not move much in frequency. A phase diagram is shown in **Figure 3**a in which the horizontal and longitudinal axis are given by Δ and Σ (the complete phase diagram is in Section D, Supporting Information). The bilayer PC slab discussed in Figure 2a locates at the origin of phase diagram, and it has two pairs of gapless linear dispersions near the K point (Figure 3b4). Along the horizontal axis, a directional bandgap is immediately obtained for a nonzero Δ (Figure 3b1). The larger the absolute value of Δ, the larger the bandgap, for example, the one presented in Figure 2c. This kind of bandgap belongs to the layer-polarized PTI and it is shaded in cyan. On the contrary, along the longitudinal axis, the frequency nodal ring exists for bilayer PC slabs with small Σ (Figure 3b5). Such nodal ring will be split out by further increasing the absolute value of Σ. Lastly, a bandgap is obtained (Figure 3b6). By further increasing the absolute value of Σ, the bandwidth of bandgap can be enlarged. One example has been illustrated in Figure 2e in which the layer-mixed PTI is found (shaded in green). The phase transition between these two kinds of layered PTIs can be found by tuning the amplitudes of broken mirror and inversion symmetry. For example, starting at the inversion symmetry breaking dominated phase (Figure 3b6), we gradually decrease the amplitude of broken inversion symmetry while increasing the amplitude of broken mirror symmetry. The second and third states meet each other (Figure 3b3), then move apart (Figure 3b2). Along with the gap closing and reopening, the topological phase transition is found.

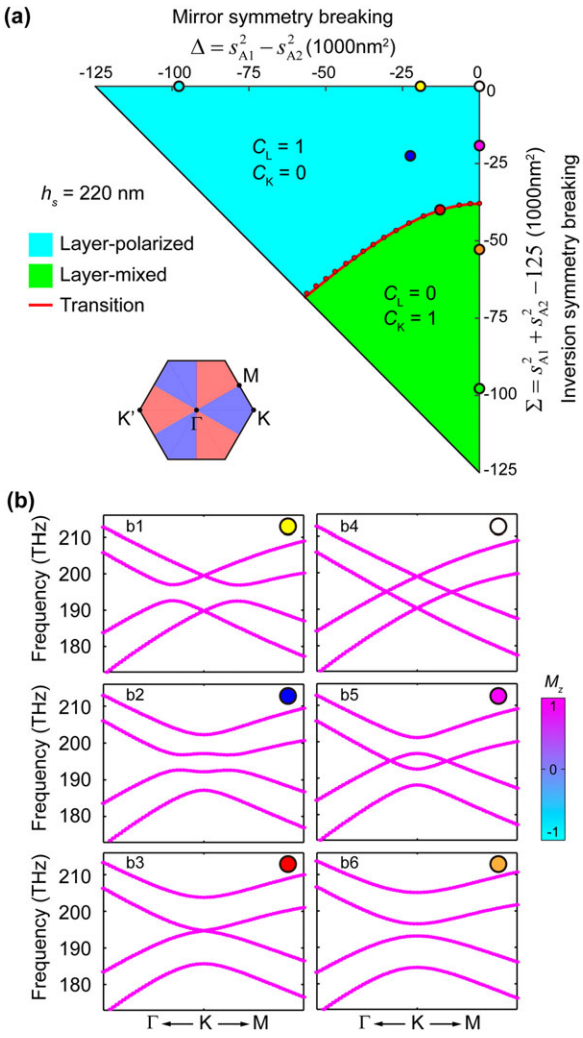

Figure 3. a) Phase diagram of AA-stacking bilayer PC slabs with the same spacer thickness of $h_s = 220$ nm but varied s_{A1} and s_{A2}. The amplitude of mirror (inversion) symmetry breaking is given by $\Delta = s_{A1}^2 - s_{A2}^2$ ($\Sigma = s_{A1}^2 + s_{A2}^2 - 125000\,\text{nm}^2$). The layer-polarized (layer-mixed) PTIs are characterized by $C_L = 1$ and $C_K = 0$ ($C_L = 0$ and $C_K = 1$) and they are shaded in cyan (green). The phase transition boundary between two topologically distinct PTIs is marked in red (small red dots for numerical results and the red curve for analytical results). Eight representative bilayer PC slabs presented in (b) and Figure 2 are labeled by big dots. The left inset shows the Brillouin zone in which one half of the Brillouin zone around the K (K′) point is shaded in blue (red). b) Bulk band structures of six representative bilayer PC slabs, showing the phase transition. Structural parameters: b1) $\Delta = 0$, $\Sigma = 0$; b2) $\Delta = 0$, $\Sigma = -19\,200\,\text{nm}^2$; b3) $\Delta = 0$, $\Sigma = -52\,800\,\text{nm}^2$; b4) $\Delta = -19\,200\,\text{nm}^2$, $\Sigma = 0$; b5) $\Delta = -22\,500\,\text{nm}^2$, $\Sigma = -22\,500\,\text{nm}^2$; b6) $\Delta = -39\,970\,\text{nm}^2$, $\Sigma = -12\,829\,\text{nm}^2$. The color of up-right dot in each subfigure is in accordance with that in (a).

The above two topological phases and associated phase transition can be described by the effective Hamiltonian of AA-stacking bilayer PC slabs with broken mirror and inversion symmetry (see detailed derivation in Section B, Supporting Information)

$$\hat{H} = f_D + v_D(\delta k_x \hat{s}_0 \hat{\sigma}_x + \delta k_y \hat{s}_0 \hat{\sigma}_y) + \eta \Delta \hat{s}_z \hat{\sigma}_z + \eta \Sigma \hat{s}_0 \hat{\sigma}_z + w \hat{s}_x \hat{\sigma}_0 \quad (1)$$

where $\delta\vec{k} = (\delta k_x, \delta k_y)$ measures from the K point. $\hat{\sigma}_i$ and $\hat{s}_i$ are the Pauli matrices acting on sub-lattice and layer spaces, respectively. In Equation (1), the second and third terms give two Dirac cones with the velocity v_D, the fourth (fifth) term describes the bandgap opening under broken mirror symmetry (broken inversion symmetry) with a gap opening coefficient η, and the last term shows the interlayer coupling strength of w. The effective Hamiltonian implies that the phase transition boundary is given by

$$\Sigma^2 = \Delta^2 + (w/\eta)^2 \tag{2}$$

where the values of w and η can be numerically fitted from the frequency spectra in Figure 2a. According to Equation (2), the red curve in Figure 3a plots the analytical phase transition boundary. The analytical results are in good agreement with those calculated by numerical simulation (red dots in Figure 3a), which in turn proves the validity of the effective Hamiltonian. According to the effective Hamiltonian presented in Equation (1), bilayer PC slabs within the phase diagram are characterized by a pair of topological indexes: C_L and C_K.[34] Here, C_L and C_K is the difference (sum) of layer-projected valley Chern numbers C_{K1} and C_{K2} where subscripts "1" and "2" correspond to eigenstates confined at layer1 and layer2, respectively. Note that C_{K1} and C_{K2} are the integrals of Berry curvatures of two lowest bulk bands within one half of the Brillouin zone around the K point (left inset of Figure 3a). In this work, valley Chern numbers at the K valley are focused on and those at the K′ valley can be obtained by considering the time-reversal symmetry. For the layer-polarized PTI in Figure 2c, $C_{K1} = 1/2$ and $C_{K2} = -1/2$, then it is characterized by the topological invariants of $C_L = C_{K1} - C_{K2} = 1$ and $C_K = C_{K1} + C_{K2} = 0$. On the contrary, the layer-mixed PTI in Figure 2e is characterized by $C_L = C_{K1} - C_{K2} = 0$ and $C_K = C_{K1} + C_{K2} = 1$ as $C_{K1} = 1/2$ and $C_{K2} = 1/2$.

5. Edge States of Domain Walls

Deterministic edge states can be found at the domain wall between two topologically distinct PTIs. We first consider the topological domain wall between the layer-polarized PTI with $C_L = 1$ (e.g., $s_{A1} = 130\,\text{nm}$ and $s_{A2} = 328.8\,\text{nm}$) and another layer-polarized PTI with $C_L = -1$ (e.g., $s_{A1} = 328.8\,\text{nm}$ and $s_{A2} = 130\,\text{nm}$) (**Figure 4**a). Its band dispersion is shown in Figure 4b in which edge states with the energy localizing near the domain wall are marked by big circles. Near the K valley (around $k_x = -2\pi/3a$), layer-direction locking edge states are observed, that is, edge states with positive group velocities have fields localizing at layer1 while edge states with negative group velocities have fields localizing at layer2 (Figure 4c). One feature of layer-direction locking edge states is the layer-dependent transmission. As shown in Figure 4d, when the source is incident from layer1 at the left end, it excites edge states whose fields localize at layer1. On the other hand, when the source is put at layer2, it excites edge states which are localized at layer2 (Figure 4e). In the above two cases, rightward edge states are excited but they belong to different valleys, that is, edge states in Figure 4d belongs to the K valley while edge states in Figure 4e belongs to the K′ valley. As edge states carry different in-plane momentums, they will be differently refracted at the termination between the bilayer PC slab and the homogeneous slab without periodic air holes (right side of the 3D schematic of Figure 4a). To out-couple edge states without the inter-valley scattering, the zigzag termination instead of the armchair termination is considered. When the source is incident from layer1, edge states at the K valley are excited. Applying the phase-matching conditions at the right terminal interface (inset of Figure 4f), edge states refract into two directional beams whose directions are indicated by two blue arrows (Figure 4f). When the source is incident from layer2, edge states also refract into two directional beams (Figure 4g). However, the refracted directions are different to those in Figure 4f because excited edge states are locked to the K′ valley instead of the K valley. With the comparison between Figure 4f,g, the selective refraction can be achieved by switching the position of incident source, that is, changing from layer1 to layer2. Note that layer-polarized edge states with fields localizing at the layer1/layer2 have y-even/y-odd symmetry (for H_z component) with respect to the plane at $y = 0$ (Figure 4c). When sharp-bends such as the Z-shape interface are considered, the y-asymmetric interface will induce the undesirable interlayer coupling and result in the propagation loss (see details in Figure S5, Supporting Information).

Another kind of topological domain walls is formed between the layer-mixed PTI with $C_K = 1$ (e.g., $s_{A1} = 130\,\text{nm}$ and $s_{A2} = 130\,\text{nm}$) and the layer-mixed PTI with $C_K = -1$ (e.g., $s_{A1} = 328.8\,\text{nm}$ and $s_{A2} = 328.8\,\text{nm}$) (**Figure 5**a). Its band dispersion is shown in Figure 5b. As the difference of C_K is 2 crossing the domain wall, two edge states with positive group velocities are found near the K valley. Figure 5c illustrates H_z fields of two representative edge states at $k_x = -2\pi/3a$, showing the layer-mixed field distributions. Since layer-mixed PTIs are dominant by the conventional valley-Hall phase, these layer-mixed edge states inside the bandgap can be guided along the sharp-bend with a low loss (see Figure S6, Supporting Information). In the following discussion, we will test another type of "robustness", that is, the high transmission along the domain wall with a large missing defect. Transmission of edge states at this domain wall is presented in Figure 5d. H_z varies alternatively in layer1 and layer2 because of the interference between two excited edge states. The oscillation length is determined by the momentum difference between two edge states. Such oscillation can be used to realize the high transmission even when a large missing defect is introduced. Here, a defected photonic waveguide with 5×6 unit cells removing at the middle of layer1 is considered. Although edge states are blocked at layer1, they can still pass along the additional channel at layer2, and the oscillation happens again after the defected cavity. High transmission of the bilayer domain wall is in a strong contrast to the low transmission of the monolayer domain wall (Figure 5e). The monolayer domain wall is constructed between a PC slab with $C_K = 1/2$ (e.g., $s_A = 130\,\text{nm}$) and another PC slab with $C_K = -1/2$ (e.g., $s_A = 328.8\,\text{nm}$). The same missing defect is also introduced at the middle of the domain wall. When edge states encounter the missing defect, they are strongly scattered and low transmission is observed at the right end of the waveguide (Figure 5f). The discussion about the transmission spectra with and without defect can be found in Section E, Supporting Information.

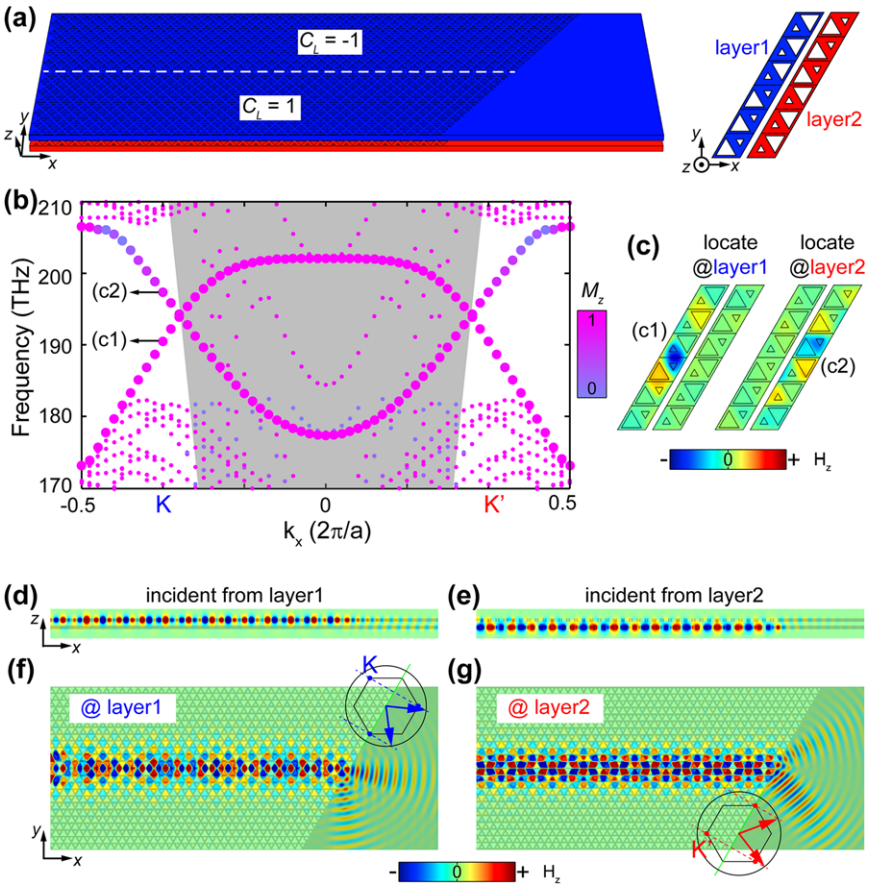

Figure 4. a) The schematics of the topological domain wall between two layer-polarized PTIs. Right insets: The 2D views of layer1 and layer2 near the boundary. b) Band dispersions of eigenstates with positive polarization factors. Big circles mark edge states while small circles mark bulk states. Near the K valley, edge states with positive (negative) group velocities are localized at layer1 (layer2). Markers of c1) and c2) indicate edge states whose eigenfields are presented in (c). Edge states near the K′ valley can be obtained by considering the time-reversal symmetry. The light cone is shaded in gray. c) H_z fields of two representative edge states at $k_x = -2\pi/3a$ with fields locating at layer1 (c1) and at layer2 (c2). d,e) Layer-dependent transmission when the source is incident from layer1 (d) and layer2 (e). f,g) Selective refracted beams when the source is incident from layer1 (f) and layer2 (g). Insets illustrate the out-coupling of edge states. Three blue (red) dots represent the K (K′) valleys in the Brillouin zone. The black circle represents the dispersion of the homogeneous bilayer slabs. Note that in (d) and (f), the operating frequency is chosen to be 190.5 THz for exciting edge states at $k_x = -2\pi/3a$ with fields locating at layer1 (corresponding to (c1) in Figure 4b), while in (e) and (g), the operating frequency is chosen to be 197.3 THz for exciting edge states at $k_x = 2\pi/3a$ with fields locating at layer2.

6. Conclusion and Discussion

In conclusion, we report all-dielectric layered PTIs by introducing the layer pseudospin into bilayer PC slabs. Layer-polarized and layer-mixed PTIs are observed, and the phase transition between them is demonstrated by a complete phase diagram. These are well illustrated by a model Hamiltonian by considering the nonzero interlayer coupling and symmetry breaking perturbations. The layer-direction locking behavior of edge states of the domain wall between layer-polarized PTIs results in selective refraction at the zigzag termination. High transmission of edge states is found at the domain wall between two layer-mixed PTIs. Methods of numerical simulations are presented in Section F, Supporting Information. Although the layer pseudospin is discussed in ref. [34] and our work, there are some differences between them (besides of the difference in the type of waves). For example, sonic crystals in ref. [34] used rigid plates for confining sound. Our proposed structures get rid of metallic plates (for confining electromagnetic waves) and focus on all-dielectric PC slabs which can be implemented in the on-chip silicon platform. In addition, the selective refraction of layer-polarized edge states and the high transmission of layer-mixed edge states against a missing defect are further discussed in our work.

A different method to implement the quantum spin Hall effect for photons has been discussed in the triangular PC whose unit cell consists of a hexagonal cluster of dielectric rods.[21] With the crystalline symmetry, the role of photonic pseudospin is played by the angular momentum of wave function. Due to the simplicity of this proposal, it has been adapted to experimentally implement for infrared photons in the uncoupled PC slab.[35] By employing the layer pseudospin, our work has demonstrated the band dispersion engineering capacity and light flow control in all-dielectric layered PTIs. The introduced bilayer PC slabs will become another platform for emulating other topological states and studying other interesting physical phenomena. For

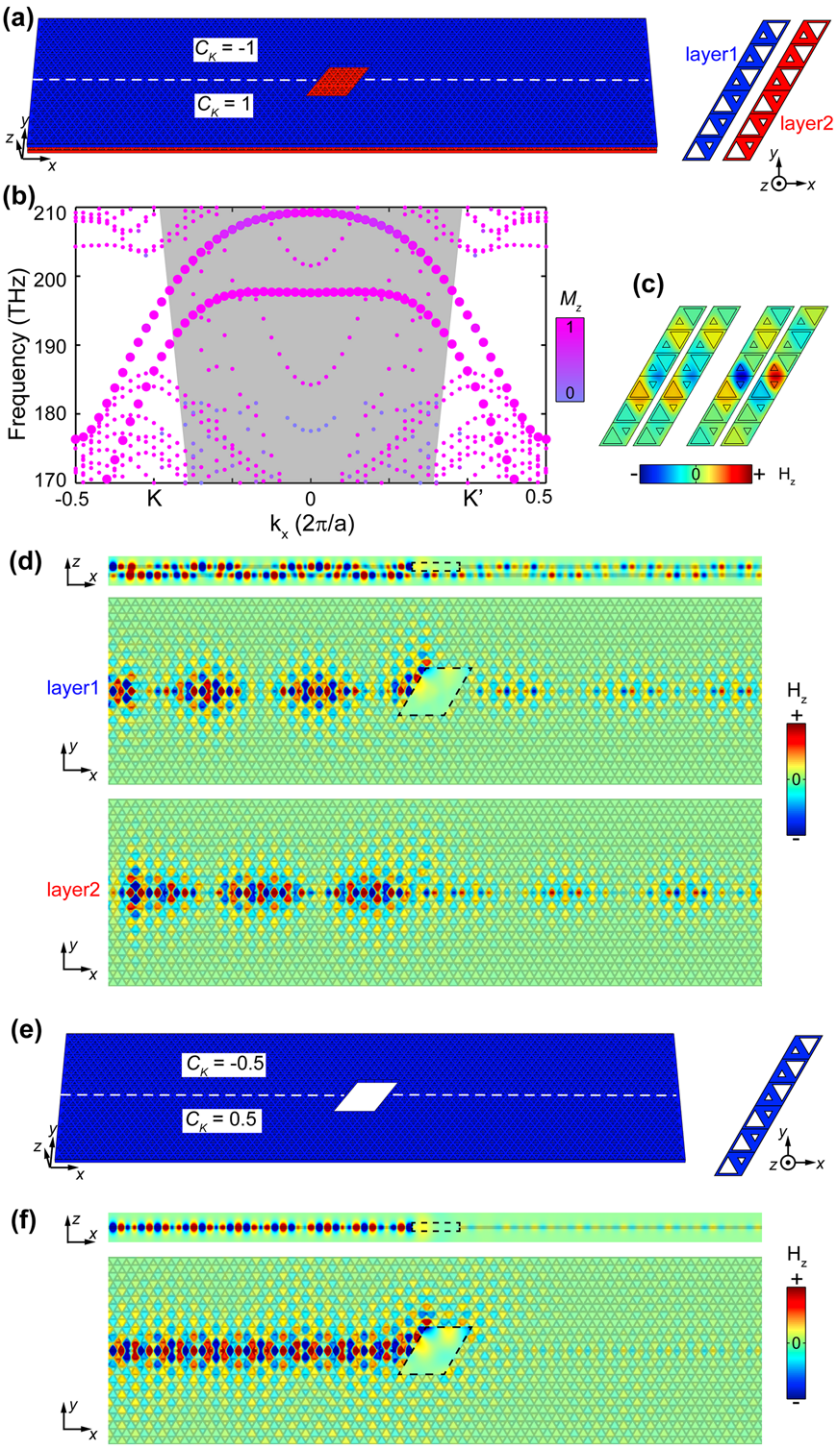

Figure 5. a) The schematics of the topological domain wall between two layer-mixed PTIs. A missing defect is introduced at the middle of layer1. Right inset: The 2D views of layer1 and layer2 near the boundary. b) Band dispersions of eigenstates with positive polarization factors. Big circles mark edge states while small circles mark bulk states. At the K (K′) valley, both edge states have positive (negative) group velocities, with fields mixing at both layers. c) H_z fields of two representative edge states at $k_x = -2\pi/3a$, showing the layer-mixed field distributions. d) Transmitted H_z fields for waveguide with a missing cavity. The oscillating fields confirm the layer-mixed property, and high transmission is observed at the right end of waveguide. e) The 3D schematics of monolayer photonic waveguides with a missing defect. Right inset: The 2D views near the boundary. f) Transmitted H_z fields, confirming low transmission in the monolayer domain wall due to the defect. In (d) and (f), the boundaries of the cavity are outlined by black dash polygons, and the operating frequency is 186.2 THz.

example, by further considering the polarization of light (e.g., TE ± TM or TE ± i × TM),[16,36] layer-spin locking behaviors can be found. Moiré-pattern-induced chiral optics can also be explored in a super-lattice by realizing a nonzero relative angle between two slabs.[37] On the other hand, photonic applications such as photonic sensors can also be achieved by filling the spacer region with tunable/active materials.[38]

Note Added: Independent of this work, the layer pseudospin was discussed in designer surface plasmon crystals where confined modes propagate on metallic surfaces.[39]

Supporting Information

Supporting Information is available from the Wiley Online Library or from the author.

Acknowledgements

X.-D.C. and X.-T.H. contributed equally to this work. This work is supported by National Natural Science Foundation of China (11704422, 61775243, 11761161002), Natural Science Foundation of Guangdong Province (2018B030308005, 2018A030310089), and Guangzhou Science, Technology and Innovation Commission (201804020029), China Postdoctoral Science Foundation (2018M633206), and the OEMT.

Conflict of Interest

The authors declare no conflict of interest.

Keywords

all-dielectric, layer pseudospin, photonic topological insulators, topological photonics

Received: March 12, 2019
Revised: May 31, 2019
Published online:

[1] J. Yuen-Zhou, S. K. Saikin, N. Y. Yao, A. Aspuru-Guzik, *Nat. Mater.* **2014**, *13*, 1026.
[2] D. Jin, L. Lu, Z. Wang, C. Fang, J. D. Joannopoulos, M. Soljačić, L. Fu, N. X. Fang, *Nat. Commun.* **2016**, *7*, 13486.
[3] R. Süsstrunk, S. D. Huber, *Science* **2015**, *349*, 47.
[4] Z. Yang, F. Gao, X. Shi, X. Lin, Z. Gao, Y. Chong, B. Zhang, *Phys. Rev. Lett.* **2015**, *114*, 114301.
[5] M. Xiao, W. Chen, W. He, C. T. Chan, *Nat. Phys.* **2015**, *11*, 920.
[6] M. Serra-Garcia, V. Peri, R. Susstrunk, O. R. Bilal, T. Larsen, L. G. Villanueva, S. D. Huber, *Nature* **2018**, *555*, 342.
[7] L. Lu, J. D. Joannopoulos, M. Soljačić, *Nat. Photonics* **2014**, *8*, 821.
[8] A. B. Khanikaev, G. Shvets, *Nat. Photonics* **2017**, *11*, 763.
[9] T. Ozawa, H. M. Price, A. Amo, N. Goldman, M. Hafezi, L. Lu, M. C. Rechtsman, D. Schuster, J. Simon, O. Zilberberg, I. Carusotto, arXiv:1802.04173, **2018**.
[10] F. Haldane, S. Raghu, *Phys. Rev. Lett.* **2008**, *100*, 013904.
[11] S. Raghu, F. Haldane, *Phys. Rev. A* **2008**, *78*, 033834.
[12] Z. Wang, Y. Chong, J. D. Joannopoulos, M. Soljačić, *Nature* **2009**, *461*, 772.
[13] M. Hafezi, E. A. Demler, M. D. Lukin, J. M. Taylor, *Nat. Phys.* **2011**, *7*, 907.
[14] G. Q. Liang, Y. D. Chong, *Phys. Rev. Lett.* **2013**, *110*, 203904.
[15] M. C. Rechtsman, J. M. Zeuner, Y. Plotnik, Y. Lumer, D. Podolsky, F. Dreisow, S. Nolte, M. Segev, A. Szameit, *Nature* **2013**, *496*, 196.
[16] A. B. Khanikaev, S. H. Mousavi, W.-K. Tse, M. Kargarian, A. H. MacDonald, G. Shvets, *Nat. Mater.* **2013**, *12*, 233.
[17] T. Ma, G. Shvets, *New J. Phys.* **2016**, *18*, 025012.
[18] W.-J. Chen, S.-J. Jiang, X.-D. Chen, B. Zhu, L. Zhou, J.-W. Dong, C. T. Chan, *Nat. Commun.* **2014**, *5*, 5782.
[19] T. Ma, A. B. Khanikaev, S. H. Mousavi, G. Shvets, *Phys. Rev. Lett.* **2015**, *114*, 127401.
[20] F. Liu, J. Li, *Phys. Rev. Lett.* **2015**, *114*, 103902.
[21] L.-H. Wu, X. Hu, *Phys. Rev. Lett.* **2015**, *114*, 223901.
[22] X.-D. Chen, F.-L. Zhao, M. Chen, J.-W. Dong, *Phys. Rev. B* **2017**, *96*, 020202(R).
[23] F. Gao, H. Xue, Z. Yang, K. Lai, Y. Yu, X. Lin, Y. Chong, G. Shvets, B. Zhang, *Nat. Phys.* **2018**, *14*, 140.
[24] M. Milićević, T. Ozawa, G. Montambaux, I. Carusotto, E. Galopin, A. Lemaître, L. Le Gratiet, I. Sagnes, J. Bloch, A. Amo, *Phys. Rev. Lett.* **2017**, *118*, 107403.
[25] K. F. Mak, K. L. McGill, J. Park, P. L. McEuen, *Science* **2014**, *344*, 1489.
[26] M. Hasan, C. Kane, *Rev. Mod. Phys.* **2010**, *82*, 3045.
[27] X.-L. Qi, S.-C. Zhang, *Rev. Mod. Phys.* **2011**, *83*, 1057.
[28] D. Xiao, W. Yao, Q. Niu, *Phys. Rev. Lett.* **2007**, *99*, 236809.
[29] X. Xu, W. Yao, D. Xiao, T. F. Heinz, *Nat. Phys.* **2014**, *10*, 343.
[30] E. V. Castro, K. S. Novoselov, S. V. Morozov, N. M. Peres, J. M. dos Santos, J. Nilsson, F. Guinea, A. K. Geim, A. H. Neto, *Phys. Rev. Lett.* **2007**, *99*, 216802.
[31] A. M. Jones, H. Yu, J. S. Ross, P. Klement, N. J. Ghimire, J. Yan, D. G. Mandrus, W. Yao, X. Xu, *Nat. Phys.* **2014**, *10*, 130.
[32] Z. Gong, G. B. Liu, H. Yu, D. Xiao, X. Cui, X. Xu, W. Yao, *Nat. Commun.* **2013**, *4*, 2053.
[33] Y. Cao, V. Fatemi, S. Fang, K. Watanabe, T. Taniguchi, E. Kaxiras, P. Jarillo-Herrero, *Nature* **2018**, *556*, 43.
[34] J. Lu, C. Qiu, W. Deng, X. Huang, F. Li, F. Zhang, S. Chen, Z. Liu, *Phys. Rev. Lett.* **2018**, *120*, 116802.
[35] S. Barik, A. Karasahin, C. Flower, T. Cai, H. Miyake, W. DeGottardi, M. Hafezi, E. Waks, *Science* **2018**, *359*, 666.
[36] C. He, X.-C. Sun, X.-P. Liu, M.-H. Lu, Y. Chen, L. Feng, Y.-F. Chen, *Proc. Natl. Acad. Sci. USA* **2016**, *113*, 4924.
[37] Z. Wu, Y. Zheng, *Adv. Opt. Mater.* **2018**, *6*, 1701057.
[38] Y. J. Lu, R. Sokhoyan, W. H. Cheng, G. Kafaie Shirmanesh, A. R. Davoyan, R. A. Pala, K. Thyagarajan, H. A. Atwater, *Nat. Commun.* **2017**, *8*, 1631.
[39] X. Wu, Z. Li, J. Chen, X. Li, J. Tian, Y. Huang, S. Wang, W. Lu, B. Hou, C. T. Chan, W. Wen, arXiv:1812.06198, **2018**.